Supporting Information

Nanotwinned Boron Suboxide (B_6O): New Ground State of B_6O

Qi An,[1] K. Madhav Reddy,[2] Huafeng Dong,[3a] Ming-Wei Chen,[2] Artem R. Oganov[3], William A. Goddard III[1*]

[1]*Materials and Process Simulation Center, California Institute of Technology, Pasadena, CA 91125, United States*

[2]*WPI Advanced Institute for Materials Research, Tohoku University, Sendai 980-8577, Japan*

[3a]*Department of Geosciences and Center for Materials by Design, Institute for Advanced Computational Science, State University of New York, Stony Brook, NY 11794-2100*

[3b]*Skolkovo Institute of Science and Technology, Skolkovo Innovation Center, 3 Nobel St., Moscow 143026, Russia.*

[3c]*Moscow Institute of Physics and Technology, 9 Institutskiy Lane, Dolgoprudny city, Moscow Region, 141700, Russian Federation*

[3d]*International Center for Materials Discovery, Northwestern Polytechnical University, Xi'an,710072, China*

[*]Corresponding author E-mail:wag@wag.caltech.edu

1. Methodology

1.1 Material fabrication and Nanoindentation

The fully dense B_6O was synthesized using hot-pressing techniques at 2173 K, 60 MPa for 1 hour. The synthesis procedure is described in detail elsewhere[1]. The TEM specimens were prepared by gently crushing and the B_6O fragments were dispersed on the holey carbon films coated copper grids.

1.2 Transmission electron microscopy

We characterized the microstructure of as-synthesized B_6O using a JEM-2100 F transmission electron microscope (JEOL Ltd. Tokyo, Japan) equipped with double spherical aberration correctors (CEOS GmbH, Heidelberg, Germany) for the image- and probe-forming lens systems. A probe convergence angle of 29 mrad was used for STEM imaging. Bright field (BF) and corresponding high-angle annular dark-field (HAADF) STEM images were simultaneously acquired.

1.3 Diffraction Simulation

Diffraction simulations were carried out using Crystal Maker® software and input files for the atomic positions for both QM-predicted R-B_6O and the τ–B_6O structures. Direct comparisons between the experimental and simulated SAED patterns (e.g. Fig 1(c) and (d); allowed us to identify both the structure and the orientation of individual grains.

1.4 Computational details

All simulations were performed used the Vienna Ab-initio Simulation Package (VASP)

periodic code with plane wave basis sets[3-5]. We used an energy cutoff of 600 eV in all the simulations since it gives excellent convergence on energy, force, stress, and geometries. We used the projector-augmented wave pseudopotentials for the Perdew–Burke–Ernzerhof (PBE) exchange-correlation functional[6]. The energy error for terminating electronic self-consistent field (SCF) and the force criterion for the geometry optimization were set equal to 10^{-6} eV and 10^{-3} eV/Å, respectively. The Monkhorst-Pack grid (8×8×8) in the *k*-space was used in the unit cell geometry optimization. Later, a smaller grid (2×2×2) and larger supercell (2×2×2) were used in the biaxial shear deformations. The Monkhorst-Pack grid (2×4×1) was used for the twinned B_6O simulations.

To examine shear deformation, we imposed the strain for a particular shear plane while allowing full structure relaxation for the other five strain components[7].

We mimic the indentation process by applying biaxial shear deformation. Here we considered the normal compressive pressure beneath the indenter and constrained the ratios of normal stress ($\boldsymbol{\sigma_{zz}}$) to shear stress ($\boldsymbol{\sigma_{xz}}$) as $\boldsymbol{\sigma_{zz}} = \boldsymbol{\sigma_{zx}} \tan\Phi$ where $\Phi = 68°$ for a Vickers indentor[8]. The residual stresses after relaxing the other strain components in both shear and biaxial shear deformations were less than 0.5 GPa.

Table S1. The predicted elastic moduli (GPa) for τ-B_6O phase from VASP.

	XX	YY	ZZ	XY	YZ	ZX
XX	582.6	75.4	89.0	0	0	0
YY	75.4	442.9	66.6	0	0	0
ZZ	89.0	66.6	563.4	0	0	0
XY	0	0	0	196.9	0	0
YZ	0	0	0	0	193.0	0
ZX	0	0	0	0	0	208.6

Table S2. The predicted elastic moduli (GPa) for 2τ-B_6O from VASP.

	XX	YY	ZZ	XY	YZ	ZX
XX	465.0	73.5	94.0	0	0	22.4
YY	73.5	563.4	83.3	0	0	10.4
ZZ	94.0	83.3	523.1	0	0	39.1
XY	0	0	0	196.3	7.8	0
YZ	0	0	0	7.8	203.7	0
ZX	22.4	10.4	39.1	0.0	0.0	213.8

Table S3. The predicted elastic moduli (GPa) for 4τ-B_6O from VASP.

	XX	YY	ZZ	XY	YZ	ZX
XX	463.9	95.7	73.4	-21.3	0	0
YY	95.7	523.2	83.8	-39.0	0	0
ZZ	73.4	83.8	561.8	-10.6	0	0
XY	-21.3	-39.0	-10.6	212.5	0	0
YZ	0	0	0	0	203.4	-8.0
ZX	0	0	0	0	-8.0	195.6

Figure S1

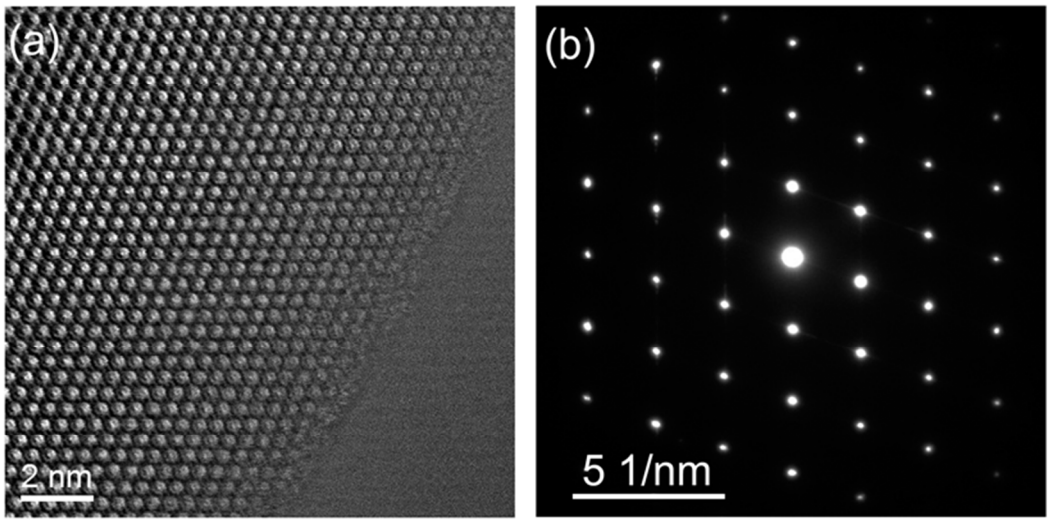

Fig. S1. STEM experimental observed for R-B_6O. (a) A representative STEM image displaying perfectly order structure (i.e., no twins and stack faults). (b) The SAED pattern obtained from the same region imaged in (a) indexed to be R-B_6O projected along the $\langle 001 \rangle_r$ zone axis.

Figure S2

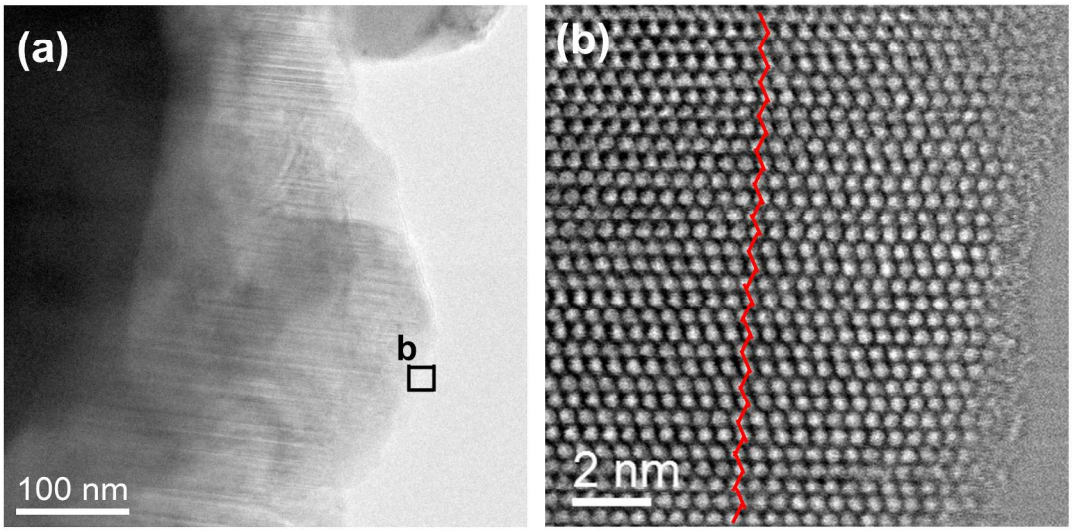

Fig. S2. The STEM images of B_6O. (a) Low-magnification STEM image. Scale bar, 100 nm. (b) Magnified TEM image showing the new τ-B6O phase. Scale bar, 2 nm.

Figure S3

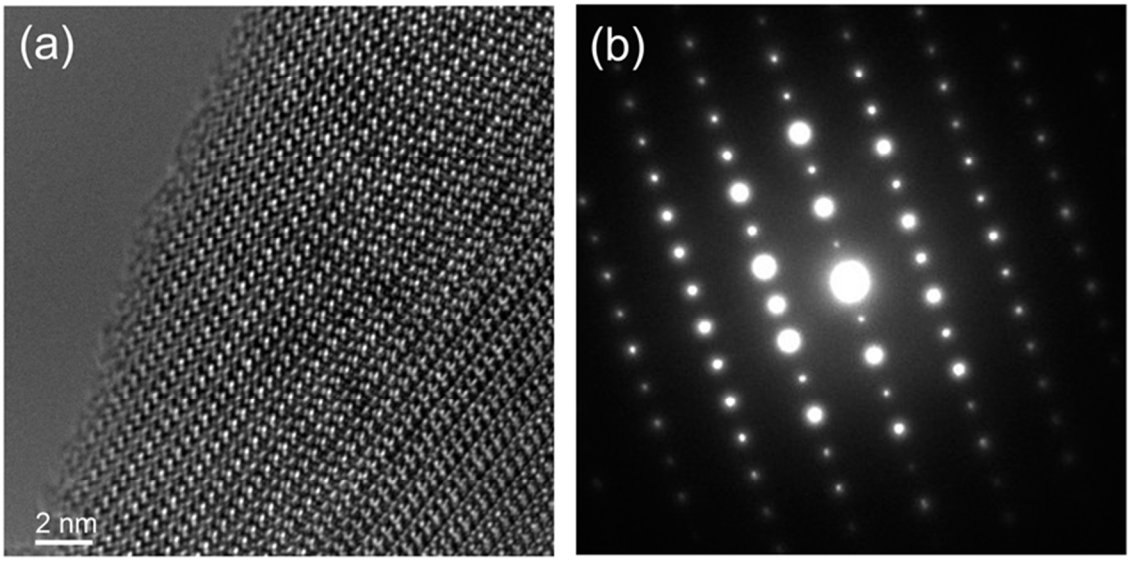

Fig. S3. HRTEM images observed for new structure τ-B_6O. (a) A representative HRTEM image displaying zig-zag nanotwinned structure (b) The SAED pattern obtained from the same region imaged in (a) indexed to be τ-B_6O.

Figure S4

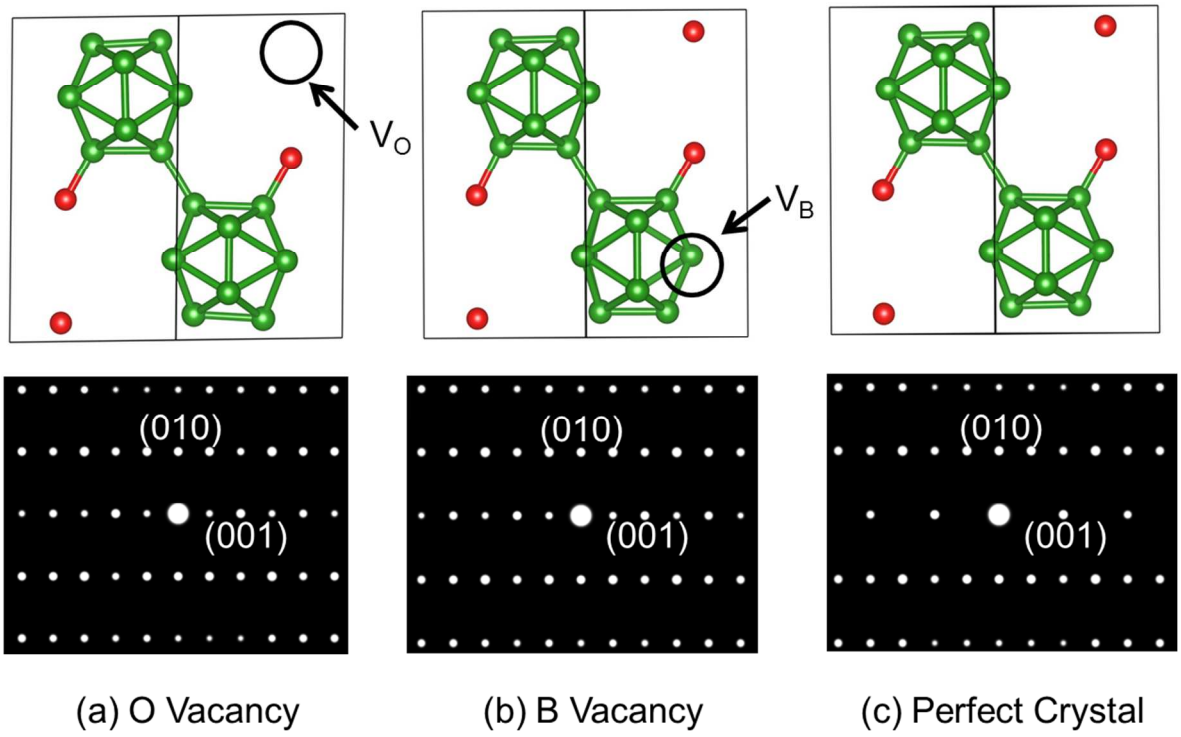

Fig. S4. The computed electron diffraction patterns of the vacancy models (B and O vacancies in the prime cell) were compared to perfect τ-B_6O. (a) B vacancy and (b) O vacancy models lead to low intensity spots between two highly strong spots. (c) Low intensity spots was not observed between highly strong spots in the perfect crystal model indicating experimental electron diffraction pattern may arise from the intrinsic defects such as vacancies due to low pressure sintering conditions carried out the as-synthesized B_6O.

Figure S5

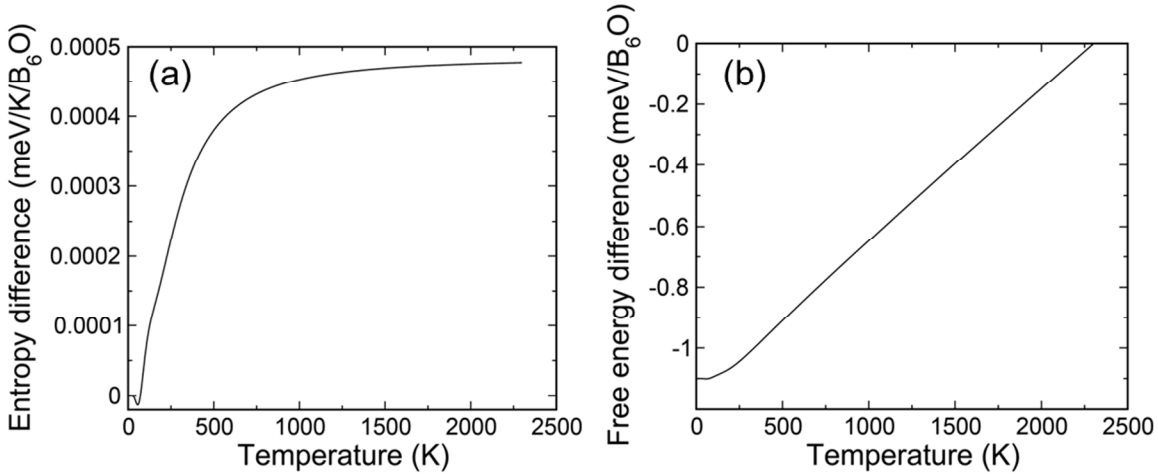

Fig. S5. The entropy (S) and Helmholtz free energy (A) difference between R-B_6O and τ-B_6O at finite temperature up to melting temperature of 2300 K. (a) Entropy difference ($S_{R\text{-}B6O}$ - $S_{\tau\text{-}B6O}$); (b) Free energy difference ($A_{R\text{-}B6O}$ - $A_{\tau\text{-}B6O}$).

Figure S6

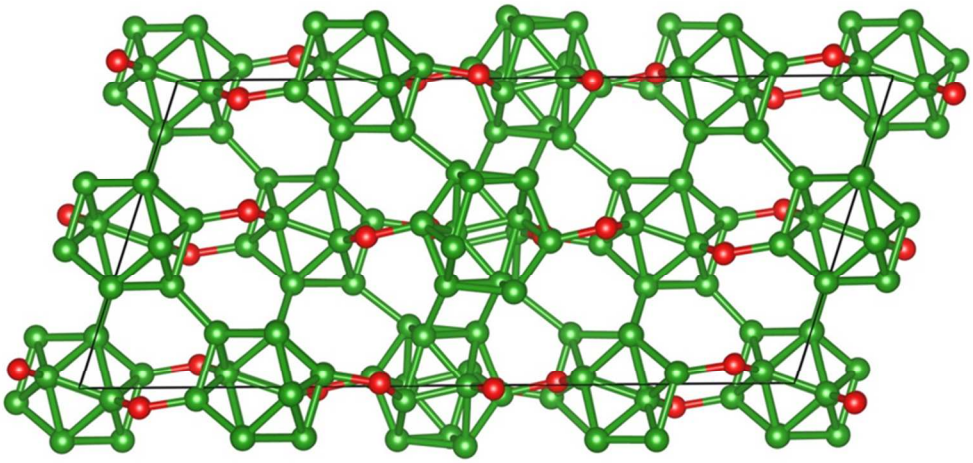

Fig. S6. The transformed structure at 0.345 strain for 2τ-B_6O phase shearing along (010)/<001> slip system.

Figure S7

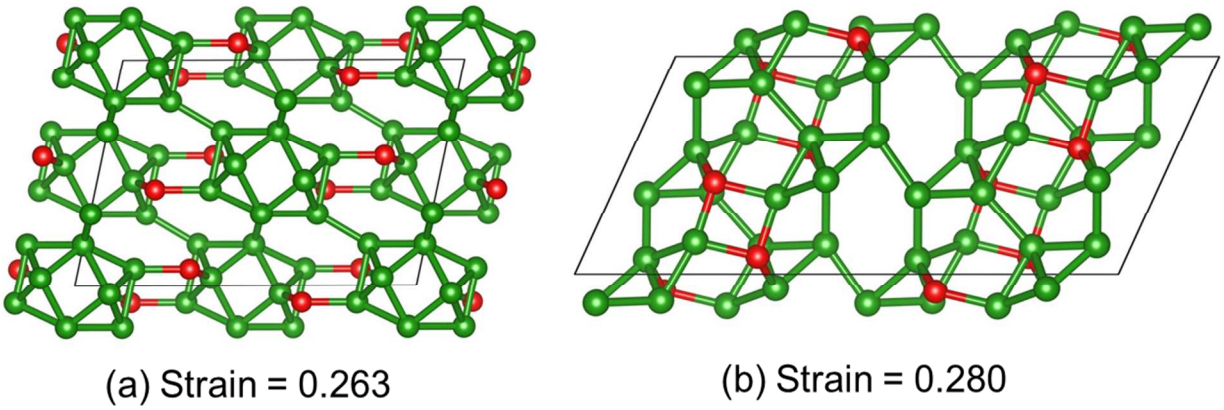

Fig. 7. The structural change for R-B_6O shear along (011)/<$2\bar{1}\bar{1}$> under indentation conditions. (a) structure at 0.263 strain before failure; (b) structure at 0.280 strain after failure.

References:

(1) Akashi, T.; Itoh, T.; Gunjishima, I.; Masumoto, H.; Goto, T. Thermoelectric properties of hot-pressed boron suboxide (B_6O). *Mater. Trans.* **2002**, *43*, 1719−1723.

(2) Guo, J.-J.; Wang, K.; Fujita, T.; McCauley, J. W.; Singh, J. P.; Chen, M.-W. Nanoindentation characterization of deformation and failure of aluminum oxynitride. *Acta Mater.* **2011**, *59*, 1671−1679.

(3) Kresse, G.; Hafner, J. Ab initio molecular dynamics for liquid metals. *Phys. Rev. B.* **1993**, *47*, 558−561.

(4) Kresse, G.; Furthmuller, J. Efficiency of ab-initio total energy calculations for metals and semiconductors using a plane-wave basis set. J. *Comput. Mater. Sci.* **1996**, *6*, 15−50.

(5) Kresse, G.; Furthmüller, J. Efficient iterative schemes for ab initio total-energy calculations using a plane-wave basis set. *Phys. Rev. B* **1996**, *16*, 11169−11186.

(6) Kresse, G.; Joubert, D. From ultrasoft pseudopotentials to the projector augmented-wave method. *Phys. Rev. B* **1999**, *59*, 1758−1775.

(7) Roundy, D.; Krenn, C. R.; Cohen, M. L.; Morris, J. W. Jr. Ideal shear strengths of fcc aluminum and copper *Phys. Rev. Lett.* **1999**, *82*, 2713−2716.

(8) Li, B.; Sun, H.; Chen, C. F. Large indentation strain-stiffening in nanotwinned cubic boron nitride. *Nat. Commun.* **2014**, *5*, 4965.